Journal of Zhejiang University-SCIENCE A (Applied Physics & Engineering)
ISSN 1673-565X (Print); ISSN 1862-1775 (Online)
www.jzus.zju.edu.cn; www.springerlink.com
E-mail: jzus@zju.edu.cn

Effects of nanoclay addition on the permeability and mechanical properties of ultra high toughness cementitious composites*

Min-jia WANG[1,2], He-dong LI[†1], Qiang ZENG[†‡2], Qing-fen CHANG[3], Xiu-shan WANG[1]
[1]*School of Civil Engineering and Architecture, Zhejiang Sci-Tech University, Hangzhou 310018, China*
[2]*College of Civil Engineering and Architecture, Zhejiang University, Hangzhou 310058, China*
[3]*Department of Architectural Engineering, Liaoyuan Vocational Technical College, Liaoyuan 136200, China*
[†]E-mail: lihedong@zstu.edu.cn; cengq14@zju.edu.cn

Received Jan. 16, 2020; Revision accepted Sept. 18, 2020; Crosschecked Nov. 17, 2020

Abstract: Tuning microstructures by adding nanoparticles is a promising way of improving the performance of cementitious composites. In this study, nanoclay was introduced to polyvinyl alcohol (PVA) fiber reinforced ultra high toughness cementitious composites (UHTCCs). The mechanical properties, crack patterns, water permeation resistance, and microstructures of UHTCCs with different dosages of nanoclay were studied. The addition of a proper dosage of nanoclay shows few effects on the compressive strength of UHTCCs, however, the compressive strength is decreased when an excessive amount of nanoclay is added. The flexural deformation capacity of UHTCCs is independent of nanoclay dosage, whereas the flexural strength generally decreases with an increasing dosage of nanoclay. Different cracking patterns were observed in the ultra high toughness cementitious composites containing nanoclay (NC-UHTCC) specimens subject to bending tests. A UHTCC with 1% (in weight) nanoclay shows the best water permeation resistance and the lowest water permeability. Variations in the mechanical properties and the water permeation resistance of UHTCCs containing different dosages of nanoclay could be ascribed to the synthetic effects of filling and heterogeneous nucleation of nanoclay at low dosages and the agglomeration effect of nanoclay at high dosages. This study is to optimize the water permeation resistance of UHTCCs, paving a path for the future application of UHTCCs in the fields of construction, decoration, and repair.

Key words: Nanoclay; Water permeability; Pore structure; Cementitious composites; Strain hardening
https://doi.org/10.1631/jzus.A2000023 **CLC number:** TU525

1 Introduction

Concrete is one of the most widely used materials in civil engineering, due to its low cost, an abundant supply of raw materials, good workability, and good durability. However, due to its quasi-brittle nature, concrete always possesses low tensile strength and low tensile strain capacity, which leads to an ease of crack formation under tension loading and thus degradation of waterproofing performance. In order to enhance the toughness and tensile strain capacity and to control the cracking behavior of concrete, many effective methods have been adopted, for instance, adding carbon-nanotube shaped reinforcement into concrete (Fan et al., 2019), or introducing various fibers with a high elastic modulus and high strain capacity into concrete (Li and Leung, 1992; Li and Obla, 1994; Li and Xu, 2011; Li et al., 2016b; Yu et al., 2018). In addition to the mechanical properties which have been widely studied, there is also a need to study

---

[‡] Corresponding author

[*] Project supported by the National Natural Science Foundation of China (No. 51978624), the Zhejiang Provincial Natural Science Foundation of China (No. LY19E080030), the Production and Construction Group's Programs for Science and Technology Development (No. 2019AB016), the Zhejiang Cultural Relics Protection Science and Technology Project (No. 2014009), the 2017 Hangzhou Transportation Society Scientific Research Project (No. 14), and the First-class Disciplines Project of Civil Engineering in Zhejiang Province, China

ORCID: Min-jia WANG, https://orcid.org/0000-0003-2954-9999; He-dong LI, https://orcid.org/0000-0002-0911-1976

the waterproof performance of fiber reinforced concrete materials.

Clay is a type of mineral with a multilayer structure with particle sizes ranging from nanoscale to microscale. It has a large water absorption rate and a large swelling rate after absorbing water (Nehdi, 2014). Clay is thus generally considered to be harmful to concrete, as its large water absorption rate would increase the water demand of fresh concrete and affect the workability and strength of concrete (Norvell et al., 2007). It is well known that nanoparticles can modify the microstructure and induce unique performance modifications of cementitious composites (Sanchez and Sobolev, 2010; Norhasri et al., 2017). The addition of nanoscale clay into cementitious composites may also lead to some unique performance modifications. Numerous studies have been conducted to investigate the effects of nanoclay-based additives on the rheological, mechanical, and transport properties of cementitious materials (Chang et al., 2007; Aly et al., 2011; Kafi et al., 2016; Papatzani, 2016; Yu et al., 2017), and many results have shown the beneficial effects of nanoclay addition with appropriate dosage on the performance of these materials. Norhasri et al. (2016) reported that nano metakaolin, as a filler, densifies the microstructure of ultra high performance concrete and leads to an enhancement of compressive strength. In a study conducted by Kuo et al. (2011), it was reported that surface-modified montmorillonite modifies the pore size distributions of cement mortars, and significantly improves the waterproof performance of cementitious composites.

Adding nanoclay into fiber reinforced cementitious composites (FRCC) is also found beneficial to the performance enhancement. Hakamy et al. (2016) reported a type of NaOH treated hemp fabric and nanoclay reinforced cementitious nanocomposite with good mechanical properties and durability. Shoukry et al. (2013) reported a type of engineered cementitious composite containing surface-modified nanoclay, which has good waterproof capability. Wei and Meyer (2014) found that replacing Portland cement with metakaolin and nanoclay leads to an increase of flexural strength and an enhancement of interfacial bonding between fibers and the cement matrix of a sisal fiber-reinforced cement composite. The focus of above studies was on the hybrid effects of nano powders and fibers on the performance of cementitious composites (Morsy et al., 2011). However, it still remains unclear how nanoclay modifies the microstructure of the cementitious matrix of FRCC, and how the nanoclay modified cementitious matrix affects cracking behavior under loading and waterproof performance under pressure. In order to address the above issues, ultra high toughness cementitious composites (UHTCCs) containing different dosages of nanoclay were designed and investigated in this study. UHTCCs are a kind of strain hardening and multiple cracking cementitious composites reinforced with no more than a 2.5% volume fraction of short random fibers, which are also known as engineered cementitious composites (ECCs) or strain hardening cement-based composites (SHCCs) (Liu et al., 2012; Huang et al., 2019; Wang et al., 2019). UHTCCs show strain hardening and multiple cracking behaviors under loading. Comprehensive experimental research and in-depth analysis were conducted to study the mechanical properties, waterproof performance, and cracking patterns of UHTCCs. These research findings are expected to be used to optimize the design of UHTCCs and to pave paths for practical applications of UHTCCs.

2 Experimental

2.1 Materials and specimen preparation

The mix proportions of the ultra high toughness cementitious composites containing nanoclay (NC-UHTCCs) studied are shown in Table 1. In order to prepare the UHTCC, 52.5R ordinary Portland cement conforming to Chinese standard GB175-2007 (AQSIQ, 2007) was used. The silica fume used was Elkem 920U Microsilica®. The fly ash used was class F and grade I conforming to GB/T 1596-2005 (AQSIQ, 2005). Previous studies (Li et al., 2016a, 2016c) suggested that the addition of a high volume of fillers could benefit the workability of fresh composites and improve the ductility and durability of UHTCCs and bring a reduction of steady state crack width after cracking. The silica sand (100–200 meshes) was used as the fine aggregate. Polycarbonate type superplasticizer (SP) was employed to adjust the workability of the fresh UHTCC. The chopped polyvinyl alcohol (PVA) fibers (2% in volume) (K-II REC15, Kuraray Co., Ltd., Japan) were added to improve the ductility of cementitious composites.

Table 1 Mix proportions of NC-UHTCCs (unit: kg/m^3)

Mix ID	Cement	Fly ash	Silica fume	Silica sand	Nanoclay	Polycarbonate superplasticizer	Polyvinyl alcohol fiber	Water
NC-UHTCC-0	250	975	25	250	0	0.3125	26	407.5
NC-UHTCC-1	250	962.5	25	250	12.5	0.3125	26	407.5
NC-UHTCC-2	250	950	25	250	25	0.625	26	407.5
NC-UHTCC-3	250	925	25	250	50	1.25	26	407.5
NC-UHTCC-4	250	900	25	250	75	2.5	26	407.5

The PVA fiber has a nominal tensile strength of 1600 MPa, a diameter of 40 μm, a length of 12 mm, a density of 1.3 g/mL, Young's modulus of 40 GPa, and an elongation capacity of 6%. The main minerals of the nanoclay (from Xingcheng City, Liaoning Province, China) used are kaolinite ($Al_2O_3{\cdot}2SiO_2{\cdot}2H_2O$), halloysite ($Al_2(OH)_4[Si_2O_5]{\cdot}nH_2O$), and montmorillonite ($(Al, Mg)_2(OH)_2[Si_4O_{10}](Na, Ca)_x{\cdot}nH_2O$). The nanoclay used is comprised of thin flakes with a mean diameter within 1 to 10 μm and a mean thickness lower than 10 nm (Fig. 1). As shown in Table 1, five nanoclay dosages, namely 0%, 1%, 2%, 4%, and 6% (in weight) of powdery materials corresponding to mix NC-UHTCC-0 to NC-UHTCC-4, respectively, were studied. In this study, nanoclay was added to replace a small fraction of fly ash. This is because when the dosage of fly ash is too high, a pozzolanic reaction of part of the fly ash will not occur and this part of the fly ash will only act as filler.

In order to prepare the UHTCCs, all required powdery materials, weighed according to Table 1, were first mixed in a planetary mixer (Hobart HL200, USA) for 60 s to avoid the possible heterogeneity of raw materials. The required amount of water was then added into the mixer followed by 3 min of fast mixing to obtain the cementitious slurry. The required amount of PVA fibers were then gradually added into the slurry followed with 3 min of further mixing. The obtained fresh cementitious composites were then cast into greased steel molds. After vibration and surface finishing, the exposed surfaces of the fresh specimens in the moulds were covered with polyethylene sheets to eliminate the rapid evaporation of water within the specimens. After a 24-h curing at (20±5) °C in moulds, all the specimens were demoulded and placed into a curing chamber for standard curing up to 28 d (temperature (20±2) °C and relative humidity >95%). Various specimens were prepared for different tests. The prism specimens of 100 mm×100 mm×400 mm were prepared for a four-point bending (FPB) test. The cubic specimens with a side length of 70.7 mm were prepared for a compression test. Conic specimens with a top side diameter of 70 mm, a bottom side diameter of 80 mm, and a height of 30 mm, were prepared for a water permeability test. The tested specimens from the compression and the FPB tests were crushed into small pieces for pore structure and microstructure observation.

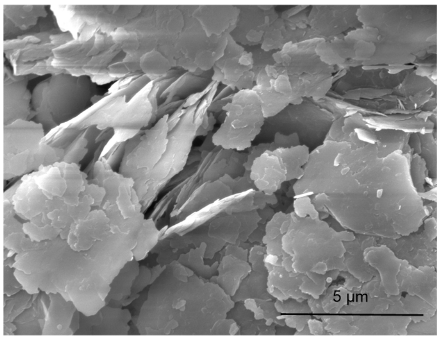

Fig. 1 Scanning electron microscope (SEM) image of nanoclay

2.2 Materials characterization tests

The compression test was performed according to the Chinese standard JGJ/T70-2009 (MOC, 2009) with a 250 kN Instron full-functional test machine at a loading rate of 0.3 MPa/s. The FPB test was conducted to assess the flexural properties of the NC-UHTCC (Fig. 2a). A tailor-made steel frame with linear variable differential transformers (LVDTs) was set on the specimens to measure the mid-span deflection. The loading and support spans were set to 100 mm and 300 mm, respectively. During the test, the loading rate was maintained at 0.2 mm/min, and an integrated measurement and control system was used to record the loading-deflection data. After the test, a pure bending section of the specimen was selected for crack analysis. The bottom surface of the

NC-UHTCC specimens was photographed with a high-resolution camera, and the cracking patterns were then analyzed with the software Image J (Schneider et al., 2012). The crack analysis procedures are described in the following. First, the RGB pictures obtained with the camera were transferred to 8-bit grey pictures (Fig. 3a). An Otsu threshold algorithm (Wang et al., 2016) was then used to segment cracks from the NC-UHTCC substrate (Fig. 3b). Generally, the segmented cracks also include pores and cavities that cannot be filtered through the threshold operation. To exclude these pores and cavities, circuits in the range of (0, 0.5) were used (Fig. 3c), which assure that the objects for imaging analysis were cracks. The width of cracks could then be measured by the gray level distribution method for a line crossing the image at a certain height (Fig. 3d). The geometric information for cracks, such as crack width distribution, could also be obtained directly from the analysis in Image J. It should be noted that the width of cracks measured with the software was significantly larger than the actual width value, since the cracks were treated with a colored solution before being photographed. The crack width comparison among different NC-UHTCCs may be meaningful but may become meaningless when compared with data from other studies.

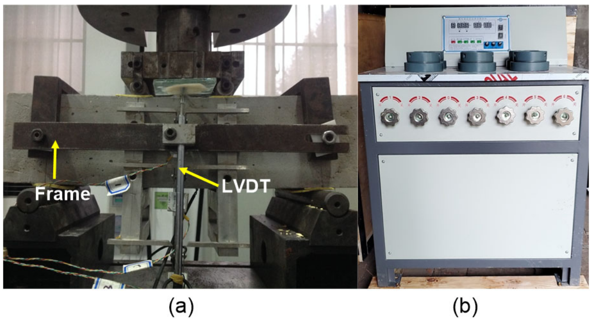

(a) (b)

Fig. 2 Setup of the FPB test (a) and the water permeability test instrument (b)

In order to evaluate the water permeation resistance of the NC-UHTCCs, water permeability tests were conducted according to the Chinese standard JGJ/T70-2009. Conic specimens were first set into

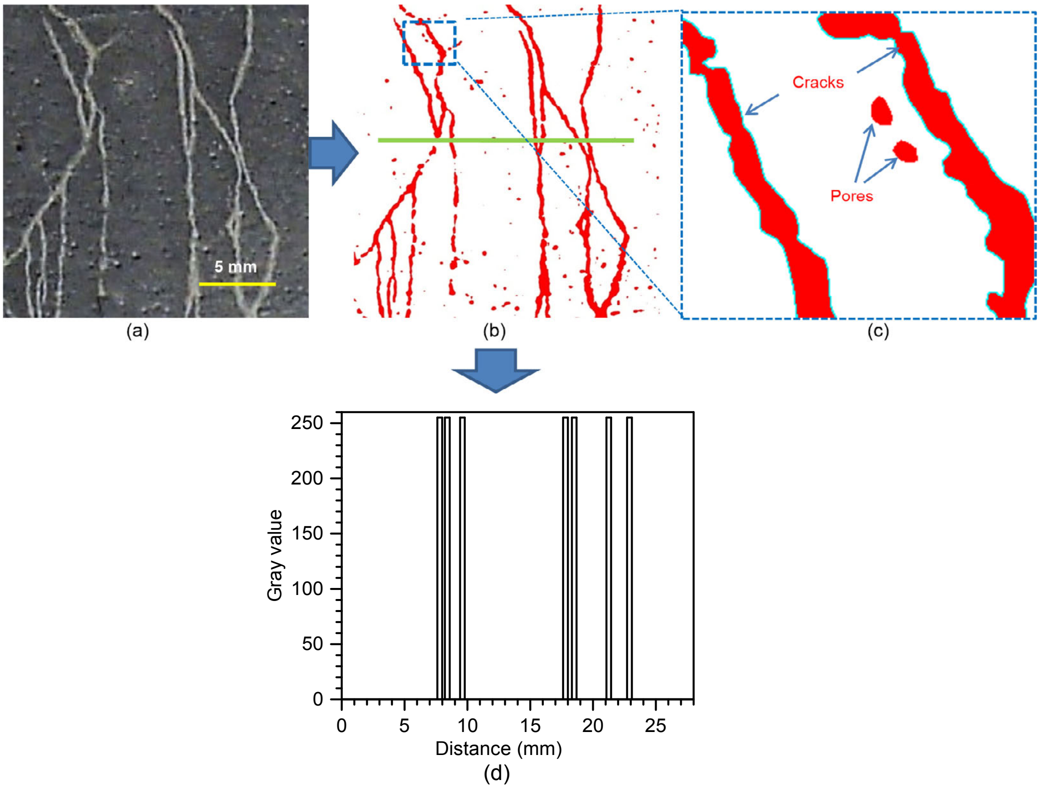

Fig. 3 Imaging analysis of the cracks in NC-UHTCC specimens subject to FPB tests

(a) Photo of a cracked NC-UHTCC specimen; (b) Image after threshold operation; (c) Exclusion of the pores from the objectives by setting the circuity in the range of (0, 0.5); (d) Gray level distribution of a line crossing the cracks shown in the panel (b) steel cones (Fig. 2b). Both the bottom and top sides of the specimen were left free, while the gap between the steel cone and the side face of the specimen was sealed with wax. This was to ensure water could not penetrate through the gap between the steel cone and the side face of the specimen. To perform the water permeability test, a water pressure of 0.2 MPa was applied slowly to equilibrium. After 2 h, the water pressure was increased by 0.1 MPa increments each time followed with an equilibrium time of 1 h. When water leakage was found for three or more specimens, testing ceased. The minimum water-leakage pressure at which water leakage was found was recorded as P_l, and the maximum survival pressure for water permeability was $P_s=P_l-0.1$. The water penetrating time t_p was equal numerically to 10 times the value of the minimum water-leakage pressure.

A mercury intrusion porosimeter (MIP) (Autopore IV 9510, Micromeritics Instrument Corporation, Norcross, GA, USA) was employed to study the pore structure of the NC-UHTCC. The minimum and maximum intrusion pressures were set to 0.54 psi (3.7 kPa) and 60 000 psi (414 MPa), respectively, and the equilibrium time for each applied pressure level was set to 10 s. An FEI Quanta FEG650 field emission environmental scanning electronic microscopy (ESEM, SU-8010, HITACHI, Japan) with an energy dispersive spectrometer (EDS, X-max80, HITACHI, Japan) was used to observe the morphology of the NC-UHTCC. The samples for the ESEM-EDS analysis were prepared with pieces from the tested FPB specimens. They were cut into an appropriate size without surface polishing to preserve the original topography of fracture surfaces. To avoid possible damage to the microstructure under high accelerating voltages and grainy images under low accelerating voltages (Zeng and Li, 2015), an accelerating voltage of 10–20 kV was applied. The spot was set to 3 and the working distance was set to 15–35 mm.

3 Results and discussion

3.1 Mechanical properties

Fig. 4 shows the compressive strengths of the 28-d measured NC-UHTCCs with various dosages of nanoclay. Each group of data in Fig. 4 is the average of three specimens. As can be seen, the UHTCC without nanoclay has a compressive strength of approximately 20 MPa, lower than that of normal concrete with a similar *w*/*b* ratio (water to binder ratio). This is because a high volume of fillers with a relatively low mechanical properties contribution was included in the UHTCC, leading to a decrease in compressive strength (Li and Xu, 2011). When a low dosage of nanoclay, for example 1%, was added, the compressive strength of the UHTCC showed almost no change. However, the compressive strength of the UHTCC decreased when more nanoclay was added.

Figs. 5a–5e show the flexural stress versus mid-span deflection curves of NC-UHTCC-0 to -4, respectively. Fig. 5f takes the median value of the flexural stress versus mid-span deflection curves of each specimen for comparison. Flexural strengths of all NC-UHTCC specimens are shown in Fig. 5g. Strain hardening behavior can be clearly observed for all specimens, indicating that nanoclay addition does not reduce the toughness of UHTCCs. The maximum mid-span deflections of all specimens are almost the same, approximately 5 mm. However, the flexural strength of NC-UHTCCs generally decreased with increasing nanoclay dosage (Figs. 5f and 5g). One possible reason is the agglomeration of nanoclay flakes (Zeng et al., 2012), which yields numerous flaws in the cementitious matrix and tends to weaken the microstructure of UHTCCs (Bastos et al., 2016; Calabria-Holley et al., 2017; Jin et al., 2017).

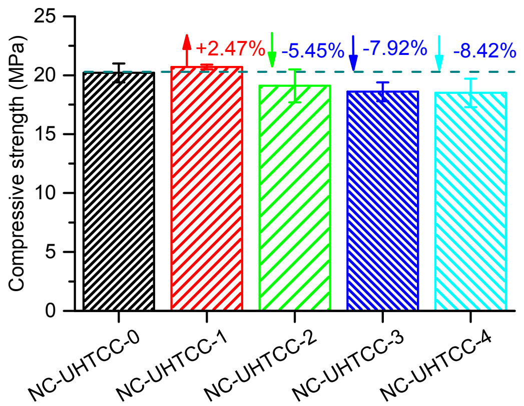

Fig. 4 Compressive strengths of NC-UHTCCs

3.2 Cracking patterns

Fig. 6 shows the images, crack patterns, and crack width distributions of NC-UHTCC specimens after FPB tests. It can be clearly seen that all the specimens show two types of cracks: main tortuous cracks and crowded cracks. The geometric characteristics of cracks were evaluated via image analysis.

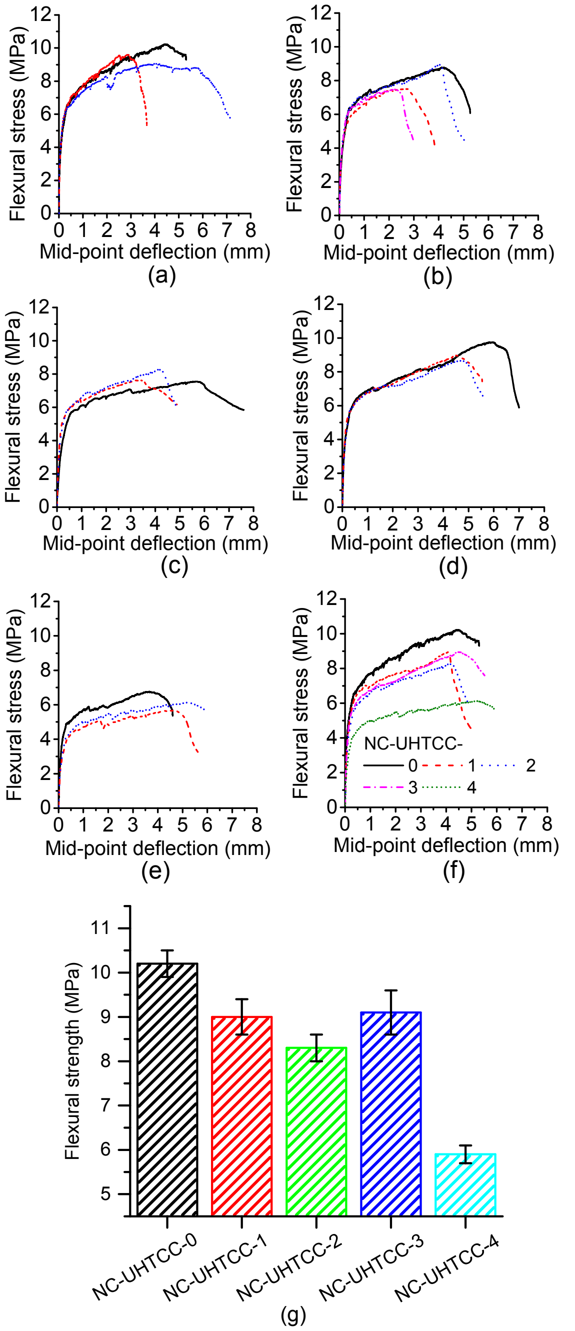

Fig. 5 Flexural stress versus mid-point deflection plots and flexural strengths of NC-UHTCCs

(a) NC-UHTCC-0; (b) NC-UHTCC-1; (c) NC-UHTCC-2; (d) NC-UHTCC-3; (e) NC-UHTCC-4; (f) Comparison of the stress-deflection plots of all NC-UHTCC specimens; (g) Flexural strengths of all NC-UHTCC specimens

Figs. 6f–6j show the patterns of crowded cracks in areas of concern. It can be seen that a clump of micro cracks generated from the bottom to the upside, forming crack bushes. The densities of cracks formed in the NC-UHTCC increased with increasing nanoclay dosage from 0% to 4% but decreased when 6% nanoclay was added. This can also be shown with the numbers of cracks at the middle height of the specimens (h=50 mm) (Table 2). The statistic widths of the crowded cracks in the bushes were in a range from 0.2 to 3 mm. The median widths of the crowded cracks were approximately 0.42 mm for NC-UHTCC-0, 0.35 mm for NC-UHTCC-1, -2, and -3, and 0.81 mm for NC-UHTCC-4 (Table 2).

The patterns of macro cracks are shown in Fig. 7. For samples NC-UHTCC-0 to -3 (Figs. 7a–7d), a single large crack (one coarse cracking tree for each specimen) can be found at the middle spans of the specimens; while for sample NC-UHTCC-4 (Fig. 7e), a cracking grove can be found in the middle area of the specimen. The cracks in the grove are thicker than those in the bushes (micro cracks) but thinner than those in the tree (coarse cracks). The obtained flexural behaviors and crack patterns of the NC-UHTCCs can be partly attributed to the interactions among the matrix, fibers, and fiber/matrix interfaces. Generally, the strain hardening feature of fiber-reinforced cementitious composites comes from the delicate balance of material parameters and their interactions (Li and Leung, 1992). The fibers can sustain the total load and transfer the load back to the matrix through interfacial shear, and cracks generate and grow in the matrix. In this way, the crowded cracks are most likely to generate in the middle span of the NC-UHTCC flexural specimens. The nanoclay addition does not seem to change the delicate balance of material parameters and their interactions, and so multiple cracking and strain hardening behaviors took place for all NC-UHTCC specimens under loading (Figs. 5 and 6). However, if the matrix is too weak, a bundle of large cracks penetrating through the width are more likely to form. This is why relatively less crowded cracks, but more coarse cracks, are observed in the NC-UHTCC-4 specimen after the FPB test.

Table 2 The number and median width of the crowded cracks at *h*=50 mm for all NC-UHTCCs

Mix ID	Number of cracks	Median width (mm)
NC-UHTCC-0	33	0.420±0.030
NC-UHTCC-1	61	0.374±0.043
NC-UHTCC-2	84	0.342±0.052
NC-UHTCC-3	91	0.369±0.046
NC-UHTCC-4	43	0.808±0.097

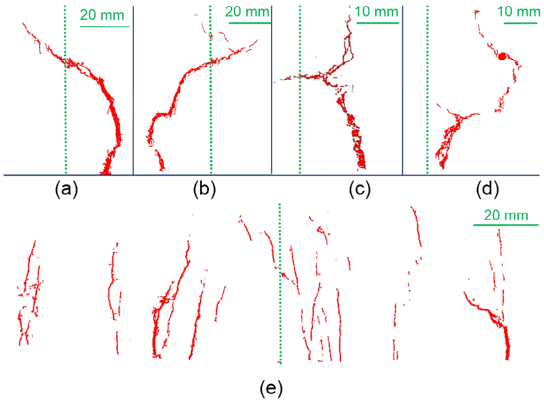

Fig. 7 Macro cracks in different specimens
(a) NC-UNTCC-0; (b) NC-UHTCC-1; (c) NCUHTCC-2; (d) NC-UHTCC-3; (e) NC-UHTCC-4. Here the vertical dashed lines represent the middle lines of NC-UHTCC specimens

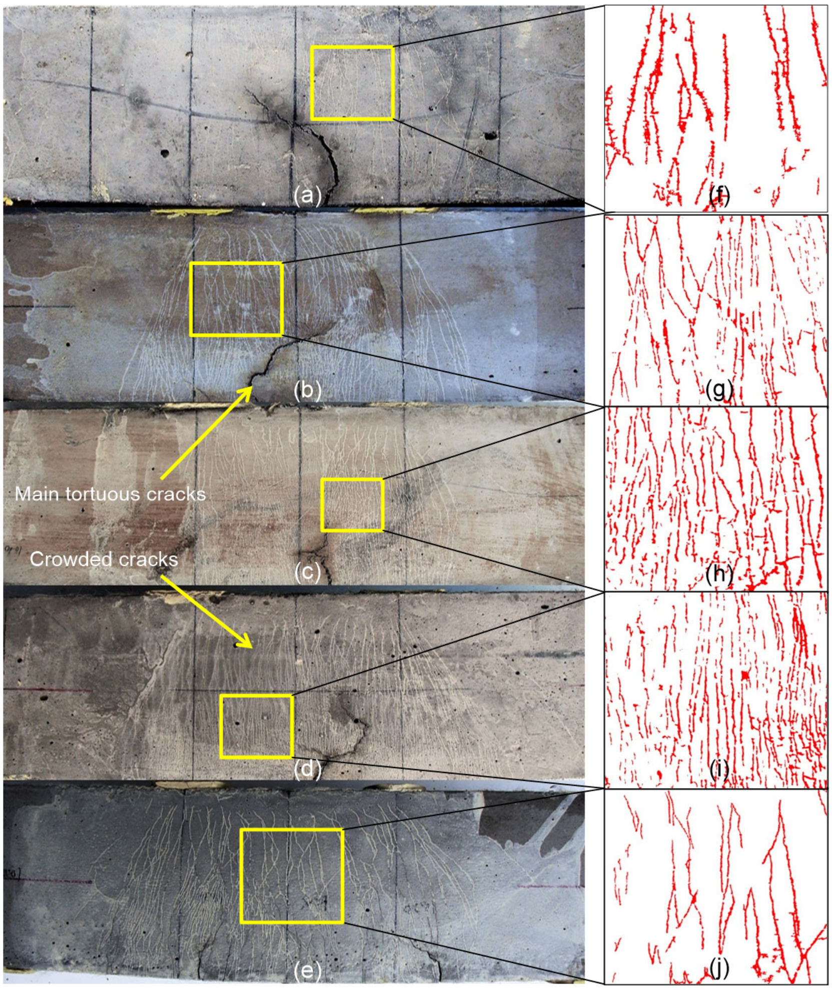

Fig. 6 Micro cracks and the results of imaging analysis
(a)–(e) Original pictures of specimens NC-UHTCC-0, -1, -2, -3, and -4 after FPB tests; (f)–(j) Figures of the areas with crowded cracks after imaging analysis of specimens NC-UHTCC-0, -1, -2, -3, and -4

3.3 Water permeability

Fig. 8 shows the water permeability test results of NC-UHTCC with different dosages of nanoclay. For NC-UHTCC-0, the maximum survival pressure P_s and the time t_p needed to penetrate through the specimen with a thickness of 30 mm are 0.8 MPa and 9 h, respectively. When 1% nanoclay was added, both P_s and t_p increased significantly, reaching 1.8 MPa and 19 h, by 125% and 111.1%, respectively. This can be attributed to the densification of the microstructure as a result of the filling and of the heterogeneous nucleation effects of nanoclay flakes (Chang et al., 2007; Kafi et al., 2016). It is well known that the solidification process of UHTCCs is a complicated physicochemical process, which includes the process of nucleation and the growth of hydrated products. During this process, the heterogeneous phases, like nanoclay, can provide nuclei sites and effectively reduce the interface energy barrier for the growth of hydration products. The hydration products hence form more easily on the surface of heterogeneous phases. Moreover, the tortuous path model—due to the flaky particles—also contributes to an increase in water permeation resistance (Nielsen, 1967; Tan and Thomas, 2016). However, when more nanoclay was added, for example 2%–6%, the P_s and t_p of the NC-UHTCC decreased. For instance, compared with NC-UHTCC-0, the P_s and t_p of NC-UHTCC-4 decreased to 0.2 MPa and 3 h, by 75% and 66.7%, respectively (Fig. 8). This indicates that the addition of a large amount of nanoclay degrades the water permeation resistance of NC-UHTCC, as a result of the agglomerations of nanoclay which is a common phenomenon in nano-sized materials. This is because nanoparticles are usually in a thermodynamically unstable state and easily agglomerate due to their relatively large surface energy. The results suggest that an appropriate dosage of nanoclay addition is beneficial to the waterproof performance of UHTCCs, but the agglomeration of nanoclay is detrimental to the waterproof performance of UHTCCs.

3.4 Morphology and microstructure

The ESEM images of the fracture surfaces of NC-UHTCC specimens are given in Fig. 9, showing the microstructure and morphology of the specimens. It can be seen that NC-UHTCC-0, -1, and -2 have a relatively dense microstructure, whereas NC-UHTCC -3 and -4 possess a porous microstructure. These observations are consistent with the change trends of compressive strength of UHTCCs, that is to say, low dosages of nanoclay addition show no effect on compressive strength, but further nanoclay addition leads to a decrease in compressive strength (Fig. 4). The particularly dense microstructure of NC-UHTCC-1 also accounts for its particularly high water permeation resistance (Fig. 8).

Massive amorphous xCaO-SiO$_2$-yH$_2$O (CSH) gels can be observed around the spherical fillers (the large spherical fillers are fly ash and the tiny ones are silica fume). Calcium hydroxide crystals with plate-like structures were rarely observed due to the pozzolanic reactions of fly ash and silica fume. It is very difficult to identify the nanoclay from the UHTCC matrix, even at a dosage of 6% (Figs. 9b–9e). This can be ascribed to the high specific surface area and the hydrophilic nature of nanoclay that facilitate the nucleation of CSH. This statement can be validated by the ESEM-EDS results of NC-UHTCC-2 (Figs. 9c and 9f), where a nanoclay flake is covered with

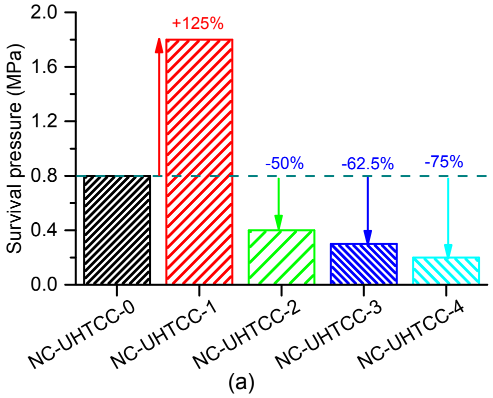

(a)

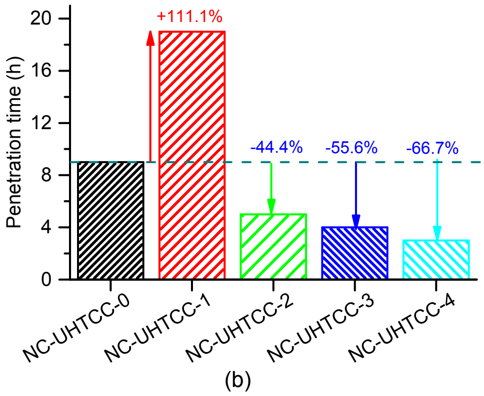

(b)

Fig. 8 Water permeability properties of NC-UHTCCs
Survival pressure (a) and time required (b) for water penetrating through the NC-UHTCC specimens

massive needle-like CSH gels. As monodispersed nanoclay flakes submerge in the nanoclay-CSH gel composites, they are thus difficult to observe directly. However, the agglomerations of nanoclay embedded in the UHTCC matrix can still be observed in the image with large magnification, as shown in Fig. 9e. The agglomerations of nano particles are caused by high superficial charges and van der Waals forces, which makes it difficult for the nano additives to be uniformly dispersed into the cementitious matrix without a dispersing agent. Studies indicate that the viscosity of natural nanoclay in an alkaline solution with a pH approximately 13 (the typical pH values of cement slurry) is much higher than that of modified ones at relatively low shear rates. High viscosity leads to strong interactions between the particles and makes particles able to sustain great shear forces (Salmas and Androutsopoulos, 2001). If no extra forces break the strong interactions, nanoclay particles agglomerate together and form clusters of nano particles in the cementitious matrix (Kafi et al., 2016; Papatzani, 2016), as shown in Fig. 9e. The agglomerations can be enhanced for their high aspect ratios (Bastos et al., 2016). The formed nano particle clusters act as flaws in the cementitious matrix, decreasing the strength and waterproof performance of the NC-UHTCC.

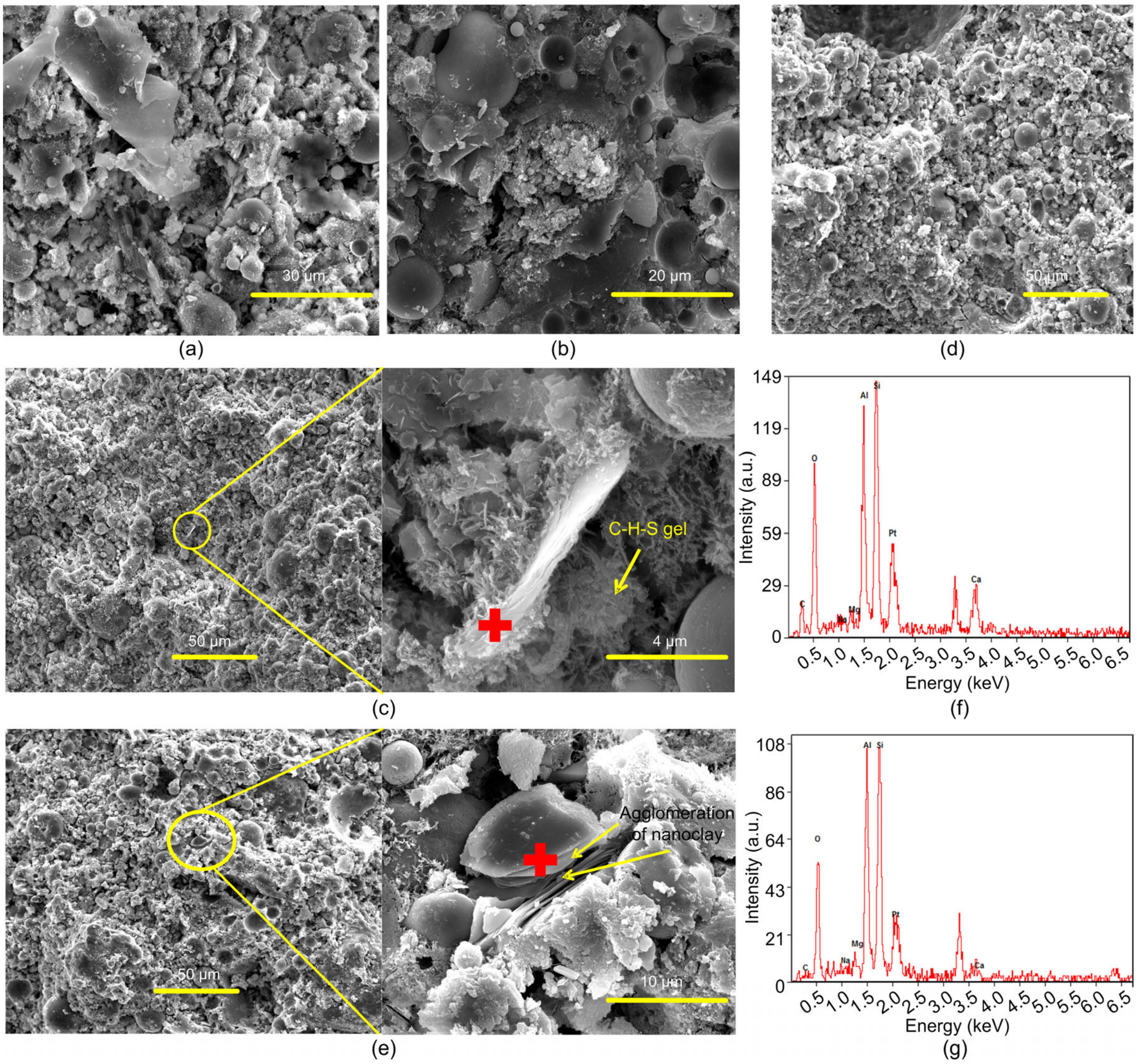

(a) (b) (d)

(c) (f)

(e) (g)

Fig. 9 ESEM-EDS results of NC-UHTCC

(a)–(e) SEM images of NC-UHTCC-0, -1, -2, -3, and -4 (the subfigures of (c) and (e) are specially investigated to illustrate the dispersion patterns); (f) and (g) EDS results of nanoclay for NC-UHTCC-2 and NC-UHTCC-4

3.5 Pore structure and its characteristics

An MIP test is always conducted to obtain information for porous materials, such as skeletal density, porosity, specific surface area, threshold pore diameter, pore size distribution (PSD), and fractal dimension (Leon y Leon, 1998). In order to evaluate the PSD of an NC-UHTCC, an MIP test was conducted. The contact angle between mercury and the pore surface, and the surface tension between vapor and liquid mercury were set to 130° and 485 N/m, respectively. According to the Washburn equation and the assumption of cylindrical pores, the minimum and maximum pore sizes corresponding to the maximum and minimum applied pressures are approximately 3 nm and approximately 300 μm, respectively. Fig. 10 shows the accumulative and differential PSD of the NC-UHTCC specimens. During the MIP test, mercury first penetrated through the spaces with relatively large size, which can be open pores, voids, cracks, or cavities. This generated the first peak of the differential PSD curves at approximately 100 μm. With the increase of applied pressure, large amounts of mercury invaded into the meso and micro spaces with a size of <1 μm, which could be small capillaries, gel pores, or confined spaces between hydrates and nanoclay. These contribute to the multi-peaks of differential PSD curves at the nanometer scale (Fig. 10b). It can be clearly seen that the PSD curves of all the UHTCC specimens show a similar pattern (Fig. 10a), which reveals that nanoclay addition did not essentially change the overall pore structures of the UHTCCs. The characteristic pore parameters of the NC-UHTCC extracted from the MIP tests are summarized in Table 3. The average skeletal density of the NC-UHTCCs was approximately 2.3 g/mL, lower than that of the CSH globules (approximately 2.6 g/mL) measured by neutron and X-ray scattering techniques (Allen et al., 2007). This can be attributed to the limited measurement scales of the MIP technique (>3 nm) and the differences in the components of hydrates between the NC-UHTCC and pure CSH. According to Table 3, approximately one third of the volume of the NC-UHTCC is pores. However, the specific pore area and threshold pore size of NC-UHTCCs vary from each other. NC-UHTCC-1 had the largest specific pore area and the lowest threshold pore size due to the densest microstructure as shown in Figs. 9 and 10. The threshold pore size is strongly relevant to the hydraulic permeability of the porous medium. No clear relationships between the characteristic pore parameters and the dosage of nanoclay can be found. It should be noted that the characteristic pore parameters of an NC-UHTCC may be biased by the simple assumption of cylindrical pores, as the microstructure of cementitious composites are rather complicated (Leon y Leon, 1998). In order to understand the complexity of the NC-UHTCC matrix, the fractal properties of the

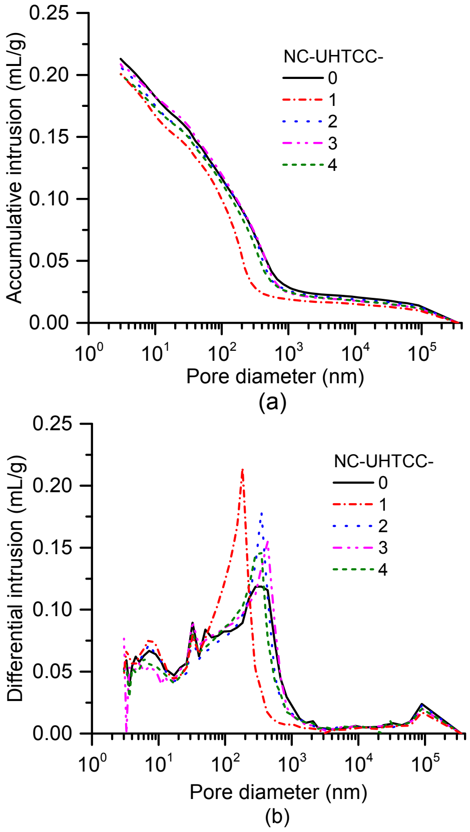

Fig. 10 Cumulative (a) and differential (b) pore size distributions of NC-UHTCCs from the intrusion phase of the MIP test

Table 3 Pore characteristics of NC-UHTCC

Specimen	Skeletal density (g/mL)	Porosity (%)	Pore area (m^2/g)	Threshold pore size (nm)
NC-UHTCC-0	2.31	32.96	33.55	350.49
NC-UHTCC-1	2.32	31.75	36.14	183.13
NC-UHTCC-2	2.29	32.09	32.89	350.06
NC-UHTCC-3	2.31	32.72	29.69	350.56
NC-UHTCC-4	2.31	31.75	30.28	350.06

NC-UHTCC were assessed. Fractal structure is the degree of occupancy of a pattern of self-similarity over a range of length scales, and this structure can be characterized by a non-integer value, named fractal dimension D (Mandelbrot, 1983). Fractal structure can influence the heterogeneous nucleation on the surfaces (Yan et al., 2016). An energy-based method was employed to evaluate the fractal dimensions based on the mercury intrusion data (Zhang and Li, 1995). In this model, a logarithm proportionality between the accumulated intrusion work W_n (J) and the accumulated mercury intrusion surface Q_n (J) was proposed, and the equation is given as follows:

$$\ln(W_n)=C+\ln(Q_n), \tag{1}$$

where C is a constant and the subscript n stands for a certain intrusion step. According to the equation $W_n=\sum_{i=1}^{n}P_iV_i$ and $Q_n=r_n^{2-D}V_n^{D/3}$, where P_i (Pa) is the pressure, V_i (m^3) is the volume of mercury intruded into the porous media, D is the surface fractal dimension of the pore surface, and r_n (m) is the pore radius. If the accumulated mercury intrusion volume V_n and the corresponding smallest radius r_n are known, the intrusion work W_n and intrusion surface Q_n can be obtained. Then, according to the following equation,

$$\ln\left(\frac{W_n}{r_n^2}\right)=C+D\ln\left(\frac{V_n^{1/3}}{r_n}\right), \tag{2}$$

the fractal dimension D can be obtained by plotting $\ln(W_n/r_n^2)$ against $\ln(V_n^{1/3}/r_n)$, as shown in Fig. 11a. Macro and micro fractal regions from the MIP data of cementitious materials can be observed (Chen et al., 2014; Li et al., 2014; Tang et al., 2017). The macro fractal region results from the special packings of clinkers, fillers, and aggregates, and the micro fractal region comes from the complicated natures of hydrates and fine admixtures. A transition zone that does not follow a fractal nature bridges the micro and macro fractal regions. Fig. 11b shows the fractal dimensions of the NC-UHTCC, which are in the range of 2.63 to 2.71. The obtained fractal dimensions approach the fractal values of ideal CSH globules according to the Jennings' CM model (D=2.67) (Jennings, 2008), although both the chemical element ratios and mineralogical components of the NC-UHTCC containing a high volume fraction of pozzolanic fillers are significantly different with the ideal CSH globules.

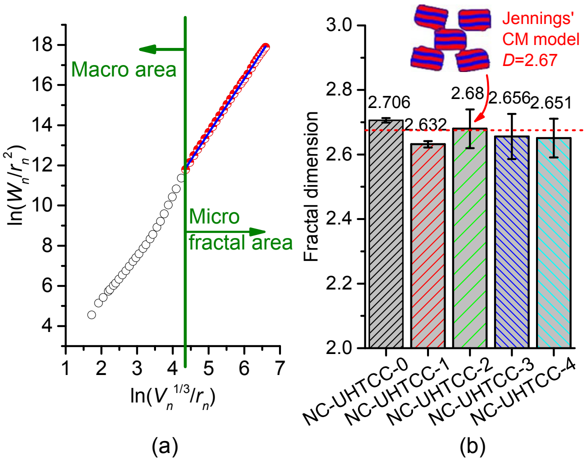

Fig. 11 Schematic illustration of the determination of the fractal dimension by the intrusion phase of the MIP test (a) and calculated fractal dimension based on the measured data (b)

3.6 Further discussion

In the above sections, except for the water permeation resistance of the NC-UHTCC that showed a significant fluctuation against the dosage of nanoclay, the strength, cracking pattern, and pore structure of the NC-UHTCCs obeyed the general rules of composites. For UHTCCs without nanoclay, there are voids among the particles of powdery materials (Fig. 12a). With appropriate mixing and dosage of nanoclay, both the filling and the heterogeneous nucleation effects of nanoclay densify the structure of cementitious matrix significantly, as shown in Figs. 10b and 12b and the threshold pore size in Table 3. Increasing the dosage of nanoclay makes the structure of cementitious matrix less dense and changes the pattern of main cracks in specimens subject to FPB tests, as a result of the agglomeration of nanoclay which increases the number of harmful large pores (Figs. 10b and 12c). While the effects of nanoclay addition on the mechanical properties and microstructure of NC-UHTCCs have been qualitatively understood, it is still unclear how the pore structures of NC-UHTCCs affect their water permeation resistance. As shown in Fig. 12d, the permeation of fluids through a cylindrical capillary and a slit cavity with the same width sees different resistance as a result of the differences in constriction. The spaces between nanoclay flakes would hence alter the transport properties of an NC-UHTCC. In this study, the hydraulic permeability of an NC-UHTCC was estimated, which was helpful in explaining the observed water permeation resistance (Fig. 8). Generally speaking, the hydraulic permeability of a porous medium is dependent on the pore structure of the porous medium. Further, the relation between the hydraulic permeability K (m^2) and the threshold pore diameter d_c ($\times10^{-6}$ m) can be described by the Katz–Thompson equation (Katz and Thompson, 1986), i.e.

$$K=\frac{Fd_c^2}{226},\tag{3}$$

where F is the permeability formation factor representing the connectivity of complex pore space. The fundamental characteristics length d_c can be directly obtained from the MIP results. The formation factor F can be determined by

$$F=\frac{\tau}{\phi},\tag{4}$$

where ϕ is the porosity and τ is the tortuosity of porous materials that is defined as the distance of continuous path between two points in the pore structure divided by their straight-line length. The tortuosity is a fundamental property for mass transfer through both the diffusion and permeation processes, as this value reflects the difficulties of mass transport in the connected pore structure (Vervoort and Cattle, 2003). Generally speaking, it is difficult to determine the value of tortuosity directly, as the real microstructure of a material and the transport paths of a fluid are unknown. Researchers often use models to evaluate the tortuosity of porous materials (Vervoort and Cattle, 2003; Amiri et al., 2005). An empirical model, as shown below, was employed in the present study to estimate the tortuosity (Salmas and Androutsopoulos, 2001):

$$\tau=A\ln\left(\frac{B}{1-\alpha_e}-1\right)-E,\tag{5}$$

where A, B, and E are constants (A=4.6242, B=4.9960, and E=5.8032), while α_e is the pore entrapment which can be directly determined from the intrusion and extrusion curves (Fig. 13a). Fig. 13b shows the tortuosity of NC-UHTCC calculated by Eq. (5). It can be found that the tortuosity of the NC-UHTCC ranges from 4.46 to 5.00 and is independent of the nanoclay dosages. The hydraulic permeability of the NC-UHTCC was calculated by Eqs. (3)–(5) and is shown in Fig. 14a. It can be seen that the permeability of NC-UHTCC-1 (approximately 2.3×10^{-15} m^2) is significantly lower than those (7.4×10^{-15} to 8.3×10^{-15} m^2) of the other samples, due to the smallest threshold pore size (183.13 nm) and the smallest porosity (31.75%) of NC-UHTCC-1 (Table 3). In addition, the monodispersed nanoclay flakes make the penetration path of water molecules through the UHTCC tortuous and increase the penetration distance of water

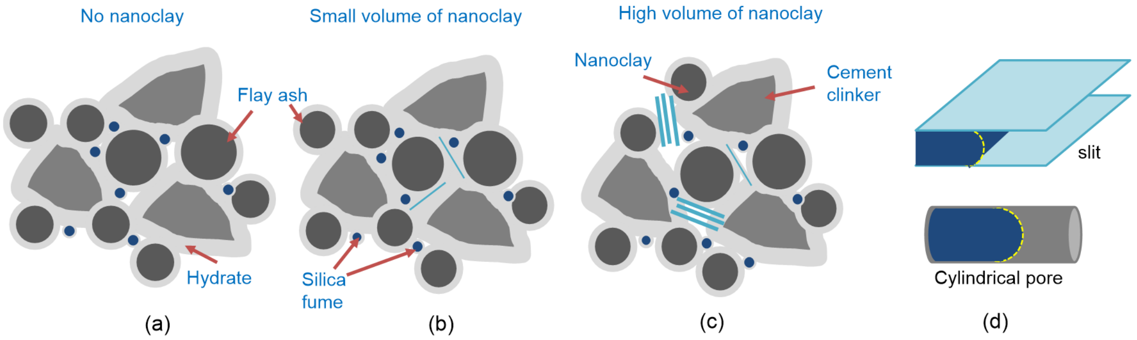

Fig. 12 Effects of nanoclay on the pore structure and water permeability of NC-UHTCCs
(a) UHTCC without nanoclay showing relatively high dense packed microstructure; (b) UHTCC with a low volume of nanoclay showing denser microstructure; (c) UHTCC with a high dosage of nanoclay having porous microstructure; (d) Schematic illustration of water permeability trough slits and cylindrical pores. Here fibers were not demonstrated in this schematic diagram

molecules, thus leading to a low permeability (Tan and Thomas, 2016). The plot of permeability against penetration time is shown in Fig. 14b. We see that the permeability is proportionally inverse to the penetration time. The lower the permeability, the longer the penetration time. It should be noted that the estimated permeability of the NC-UHTCC is a somewhat rough estimate. This is because the Katz-Thompson model oversimplifies the permeation processes. There is a need for more research to improve the material properties of nanoclay modified cementitious composites in the future.

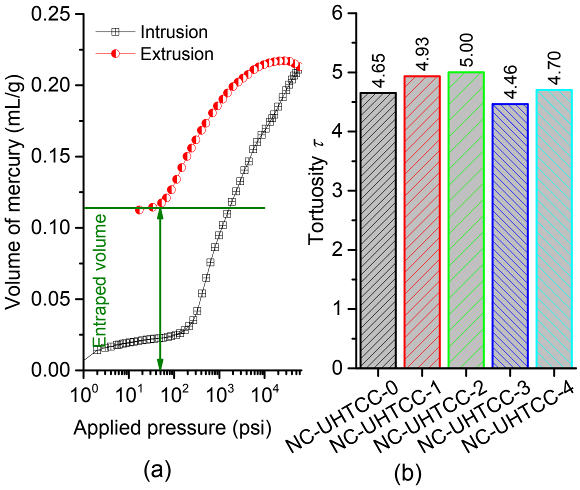

(a) (b)

Fig. 13 Schematic illustration of the entrapment of mercury by MIP (a) and calculated tortuosity based on the entrapment fraction (1 psi=6.895 kPa) (b)

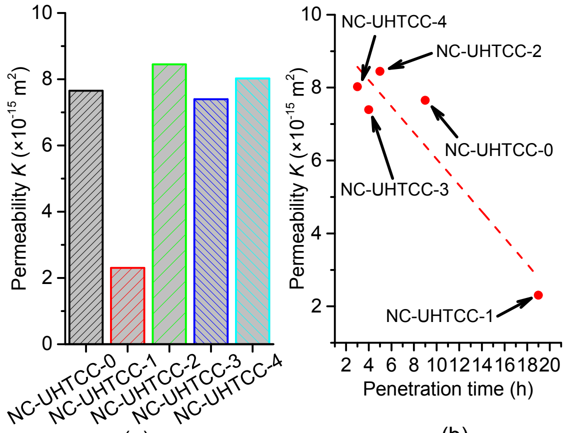

(a) (b)

Fig. 14 Hydraulic permeability of NC-UHTCCs predicted from the entrapment data (a) and relationship between hydraulic permeability and penetration time (b)

4 Conclusions

In this study, UHTCCs containing different dosages of nanoclay were prepared and investigated. The mechanical properties, cracking patterns, water permeation resistance, and microstructures of UHTCCs were evaluated by conducting compression tests, FPB tests, water permeability tests, MIP tests, and SEM observations, and the findings are discussed. According to the results, the following points can be highlighted:

1. Addition of 1% nanoclay shows few effects to the compressive strength of UHTCCs, while a further increase of nanoclay dosage results in a continuous decrease of compressive strength. The flexural strength of NC-UHTCCs decreases from approximately 10 MPa to approximately 6 MPa with the dosage of nanoclay increasing from 0% to 6%. The maximum mid-span deflections of all UHTCC were almost the same, approximately 5 mm, indicating that the introduction of a proper dosage of nanoclay would not degrade the flexural deformation capacity of UHTCCs.

2. Compared with other samples, a UHTCC containing 1% nanoclay has the smallest porosity of 31.75% and a threshold pore size of 183.13 nm, but the highest survival pressure P_s of 1.8 MPa and the largest penetration time t_p of 19 h. The excellent water permeation resistance of a UHTCC containing 1% nanoclay can be attributed to the refined microstructure due to the filling and heterogeneous nuclei effects of nanoclay and the tortuous penetration path of water molecules caused by the monodispersed nanoclay flakes. However, excessive nanoclay (>2%) addition would induce the agglomeration of nanoclay and the formation of nanoclay clusters which act as flaws in the cementitious matrix, leading to a decrease in the water permeation resistance of UHTCCs.

Contributors

He-dong LI designed the research. Min-jia WANG and Xiu-shan WANG finished the experiments. Min-jia WANG processed the corresponding data. Qiang ZENG wrote the first draft of the manuscript. Qing-fen CHANG helped to organize the manuscript. He-dong LI and Min-jia WANG revised and edited the final version.

Conflict of interest

Min-jia WANG, He-dong LI, Qiang ZENG, Qing-fen CHANG, and Xiu-shan WANG declare that they have no conflict of interest.

Reference

Allen AJ, Thomas JJ, Jennings HM, 2007. Composition and density of nanoscale calcium–silicate–hydrate in cement. *Nature Materials*, 6(4):311-316.
https://doi.org/10.1038/nmat1871

Aly M, Hashmi MSJ, Olabi AG, et al., 2011. Effect of nano clay particles on mechanical, thermal and physical behaviours of waste-glass cement mortars. *Materials Science and Engineering: A*, 528(27):7991-7998.
https://doi.org/10.1016/j.msea.2011.07.058

Amiri O, Aït-Mokhtar A, Sarhani M, 2005. Tri-dimensional modelling of cementitious materials permeability from polymodal pore size distribution obtained by mercury intrusion porosimetry tests. *Advances in Cement Research*, 17(1):39-45.
https://doi.org/10.1680/adcr.2005.17.1.39

AQSIQ (State General Administration of the People's Republic of China for Quality Supervision and Inspection and Quarantine), 2005. Fly Ash Used for Cement and Concrete, GB/T 1596-2005. Standardization Administration of the People's Republic of China, Beijing, China (in Chinese).

AQSIQ (State General Administration of the People's Republic of China for Quality Supervision and Inspection and Quarantine), 2007. Common Portland Cement, GB175-2007. Standardization Administration of the People's Republic of China, Beijing, China (in Chinese).

Bastos G, Patiño-Barbeito F, Patiño-Cambeiro F, et al., 2016. Nano-inclusions applied in cement-matrix composites: a review. *Materials*, 9(12):1015.
https://doi.org/10.3390/ma9121015

Calabria-Holley J, Papatzani S, Naden B, et al., 2017. Tailored montmorillonite nanoparticles and their behaviour in the alkaline cement environment. *Applied Clay Science*, 143: 67-75.
https://doi.org/10.1016/j.clay.2017.03.005

Chang TP, Shih JY, Yang KM, et al., 2007. Material properties of Portland cement paste with nano-montmorillonite. *Journal of Materials Science*, 42(17):7478-7487.
https://doi.org/10.1007/s10853-006-1462-0

Chen XD, Wu SX, Zhou JK, 2014. Experimental study and analytical model for pore structure of hydrated cement paste. *Applied Clay Science*, 101:159-167.
https://doi.org/10.1016/j.clay.2014.07.031

Fan LF, Wang LJ, Ma GW, et al., 2019. Enhanced compressive performance of concrete via 3D-printing reinforcement. *Journal of Zhejiang University-SCIENCE A (Applied Physics & Engineering)*, 20(9):675-684.
https://doi.org/10.1631/jzus.A1900135

Hakamy A, Shaikh FUA, Low IM, 2016. Effect of calcined nanoclay on the durability of NaOH treated hemp fabric-reinforced cement nanocomposites. *Materials & Design*, 92:659-666.
https://doi.org/10.1016/j.matdes.2015.12.097

Huang BT, Li QH, Xu SL, et al., 2019. Static and fatigue performance of reinforced concrete beam strengthened with strain-hardening fiber-reinforced cementitious composite. *Engineering Structures*, 199:109576.
https://doi.org/10.1016/j.engstruct.2019.109576

Jennings HM, 2008. Refinements to colloid model of C-S-H in cement: CM-II. *Cement and Concrete Research*, 38(3): 275-289.
https://doi.org/10.1016/j.cemconres.2007.10.006

Jin SS, Zhang JX, Han S, 2017. Fractal analysis of relation between strength and pore structure of hardened mortar. *Construction and Building Materials*, 135:1-7.
https://doi.org/10.1016/j.conbuildmat.2016.12.152

Kafi MA, Sadeghi-Nik A, Bahari A, et al., 2016. Microstructural characterization and mechanical properties of cementitious mortar containing montmorillonite nanoparticles. *Journal of Materials in Civil Engineering*, 28(12): 04016155.
https://doi.org/10.1061/(ASCE)MT.1943-5533.0001671

Katz AJ, Thompson AH, 1986. Quantitative prediction of permeability in porous rock. *Physical Review B*, 34(11): 8179-8181.
https://doi.org/10.1103/PhysRevB.34.8179

Kuo WY, Huang JS, Yu BY, 2011. Evaluation of strengthening through stress relaxation testing of organo-modified montmorillonite reinforced cement mortars. *Construction and Building Materials*, 25(6):2771-2776.
https://doi.org/10.1016/j.conbuildmat.2011.01.001

Leon y Leon CA, 1998. New perspectives in mercury porosimetry. *Advances in Colloid and Interface Science*, 76-77:341-372.
https://doi.org/10.1016/S0001-8686(98)00052-9

Li HD, Xu SL, 2011. Determination of energy consumption in the fracture plane of ultra high toughness cementitious composite with direct tension test. *Engineering Fracture Mechanics*, 78(9):1895-1905.
https://doi.org/10.1016/j.engfracmech.2011.03.012

Li KF, Zeng Q, Luo MY, et al., 2014. Effect of self-desiccation on the pore structure of paste and mortar incorporating 70% GGBS. *Construction and Building Materials*, 51: 329-337.
https://doi.org/10.1016/j.conbuildmat.2013.10.063

Li QH, Huang BT, Xu SL, et al., 2016a. Compressive fatigue damage and failure mechanism of fiber reinforced cementitious material with high ductility. *Cement and Concrete Research*, 90:174-183.
https://doi.org/10.1016/j.cemconres.2016.09.019

Li QH, Zhao X, Xu SL, et al., 2016b. Influence of steel fiber on dynamic compressive behavior of hybrid fiber ultra high toughness cementitious composites at different strain rates. *Construction and Building Materials*, 125:490-500.
https://doi.org/10.1016/j.conbuildmat.2016.08.066

Li QH, Gao X, Xu SL, 2016c. Multiple effects of nano-SiO_2 and hybrid fibers on properties of high toughness fiber reinforced cementitious composites with high-volume fly ash. *Cement and Concrete Composites*, 72:201-212.
https://doi.org/10.1016/j.cemconcomp.2016.05.011

Li VC, Leung CKY, 1992. Steady-state and multiple cracking

of short random fiber composites. *Journal of Engineering Mechanics*, 118(11):2246-2264.
https://doi.org/10.1061/(asce)0733-9399(1992)118:11(2246)

Li VC, Obla KH, 1994. Effect of fiber length variation on tensile properties of carbon-fiber cement composites. *Composites Engineering*, 4(9):947-964.
https://doi.org/10.1016/0961-9526(94)90037-X

Liu W, Xu SL, Li QH, 2012. Experimental study on fracture performance of ultra-high toughness cementitious composites with *J*-integral. *Engineering Fracture Mechanics*, 96:656-666.
https://doi.org/10.1016/j.engfracmech.2012.09.007

Mandelbrot BB, 1983. The Fractal Geometry of Nature. WH Freeman, New York, USA, p.14-20.

MOC (Ministry of Construction of the People's Republic of China), 2009. Standard for Test Method of Performance on Building Mortar, JGJ/T70-2009. MOC, Beijing, China (in Chinese).

Morsy MS, Alsayed SH, Aqel M, 2011. Hybrid effect of carbon nanotube and nano-clay on physico-mechanical properties of cement mortar. *Construction and Building Materials*, 25(1):145-149.
https://doi.org/10.1016/j.conbuildmat.2010.06.046

Nehdi ML, 2014. Clay in cement-based materials: critical overview of state-of-the-art. *Construction and Building Materials*, 51:372-382.
https://doi.org/10.1016/j.conbuildmat.2013.10.059

Nielsen LE, 1967. Models for the permeability of filled polymer systems. *Journal of Macromolecular Science: Part A-Chemistry*, 1(5):929-942.
https://doi.org/10.1080/10601326708053745

Norhasri MSM, Hamidah MS, Fadzil AM, et al., 2016. Inclusion of nano metakaolin as additive in ultra high performance concrete (UHPC). *Construction and Building Materials*, 127:167-175.
https://doi.org/10.1016/j.conbuildmat.2016.09.127

Norhasri MSM, Hamidah MS, Fadzil AM, 2017. Applications of using nano material in concrete: a review. *Construction and Building Materials*, 133:91-97.
https://doi.org/10.1016/j.conbuildmat.2016.12.005

Norvell JK, Stewart JG, Juenger MC, et al., 2007. Influence of clays and clay-sized particles on concrete performance. *Journal of Materials in Civil Engineering*, 19(12):1053-1059.
https://doi.org/10.1061/(asce)0899-1561(2007)19:12(1053)

Papatzani S, 2016. Effect of nanosilica and montmorillonite nanoclay particles on cement hydration and microstructure. *Materials Science and Technology*, 32(2):138-153.
https://doi.org/10.1179/1743284715Y.0000000067

Salmas CE, Androutsopoulos GP, 2001. A novel pore structure tortuosity concept based on nitrogen sorption hysteresis data. *Industrial & Engineering Chemistry Research*, 40(2):721-730.
https://doi.org/10.1021/ie000626y

Sanchez F, Sobolev K, 2010. Nanotechnology in concrete-a review. *Construction and Building Materials*, 24(11): 2060-2071.
https://doi.org/10.1016/j.conbuildmat.2010.03.014

Schneider CA, Rasband WS, Eliceiri KW, 2012. NIH Image to ImageJ: 25 years of image analysis. *Nature Methods*, 9(7):671-675.
https://doi.org/10.1038/nmeth.2089

Shoukry H, Kotkata MF, Abo-el-Enein SA, et al., 2013. Flexural strength and physical properties of fiber reinforced nano metakaolin cementitious surface compound. *Construction and Building Materials*, 43:453-460.
https://doi.org/10.1016/j.conbuildmat.2013.02.030

Tan B, Thomas NL, 2016. A review of the water barrier properties of polymer/clay and polymer/graphene nanocomposites. *Journal of Membrane Science*, 514:595-612.
https://doi.org/10.1016/j.memsci.2016.05.026

Tang SW, He Z, Cai XH, et al., 2017. Volume and surface fractal dimensions of pore structure by NAD and LT-DSC in calcium sulfoaluminate cement pastes. *Construction and Building Materials*, 143:395-418.
https://doi.org/10.1016/j.conbuildmat.2017.03.140

Vervoort RW, Cattle SR, 2003. Linking hydraulic conductivity and tortuosity parameters to pore space geometry and pore-size distribution. *Journal of Hydrology*, 272(1-4): 36-49.
https://doi.org/10.1016/S0022-1694(02)00253-6

Wang RZ, Li DY, Wang XR, et al., 2019. A novel and convenient temperature dependent fracture strength model for the laminated ultra-high temperature ceramic composites. *Journal of Alloys and Compounds*, 771:9-14.
https://doi.org/10.1016/j.jallcom.2018.08.253

Wang ZD, Zeng Q, Wang L, et al., 2016. Characterizing frost damages of concrete with flatbed scanner. *Construction and Building Materials*, 102:872-883.
https://doi.org/10.1016/j.conbuildmat.2015.11.029

Wei JQ, Meyer C, 2014. Sisal fiber-reinforced cement composite with Portland cement substitution by a combination of metakaolin and nanoclay. *Journal of Materials Science*, 49(21):7604-7619.
https://doi.org/10.1007/s10853-014-8469-8

Yan DM, Zeng Q, Xu SL, et al., 2016. Heterogeneous nucleation on concave rough surfaces: thermodynamic analysis and implications for nucleation design. *The Journal of Physical Chemistry C*, 120(19):10368-10380.
https://doi.org/10.1021/acs.jpcc.6b01693

Yu J, Li HD, Leung CKY, et al., 2017. Matrix design for waterproof engineered cementitious composites (ECCs). *Construction and Building Materials*, 139:438-446.
https://doi.org/10.1016/j.conbuildmat.2017.02.076

Yu KQ, Yu JT, Dai JG, et al., 2018. Development of ultra-high performance engineered cementitious composites using polyethylene (PE) fibers. *Construction and Building Materials*, 158:217-227.
https://doi.org/10.1016/j.conbuildmat.2017.10.040

Zeng Q, Li KF, 2015. Reaction and microstructure of cement–

fly-ash system. *Materials and Structures*, 48(6):1703-1716.
https://doi.org/10.1617/s11527-014-0266-y

Zeng Q, Li KF, Fen-Chong T, et al., 2012. Determination of cement hydration and pozzolanic reaction extents for fly-ash cement pastes. *Construction and Building Materials*, 27(1):560-569.
https://doi.org/10.1016/j.conbuildmat.2011.07.007

Zhang BQ, Li SF, 1995. Determination of the surface fractal dimension for porous media by mercury porosimetry. *Industrial & Engineering Chemistry Research*, 34(4):1383-1386.
https://doi.org/10.1021/ie00043a044

中文概要

题　目：纳米级粘土对超高韧性水泥基复合材料渗透性和力学性能的影响

目　的： 1. 通过添加纳米级粘土以调节超高韧性水泥基复合材料（UHTCC）的微观结构，从而提高其抗渗性能。2. 研究不同用量的纳米级粘土对 UHTCC 的力学性能、裂纹形态、孔结构、孔隙率及渗透性的影响规律，并阐释其抗渗机理。

创新点： 1. 通过控制纳米级粘土的掺量，在不明显降低抗压强度的前提下，明显改善 UHTCC 的抗渗性能；2. 通过综合分析孔结构、试件受弯裂缝和跨中挠度等，揭示粘土掺量对 UHTCC 的力学性能及抗渗性能的影响规律。

方　法： 综合利用轴压试验、四点弯曲试验、抗渗试验、压汞试验和扫描电镜微观观测，系统分析纳米粘土用量对 UHTCC 的抗压强度、弯曲性能、孔结构及抗渗性能的影响，并尝试阐明抗渗性能提升机理。

结　论： 1. 添加质量分数为 1%的纳米级粘土对 UHTCC 的抗压强度几乎没有影响；超过该用量，材料的抗压强度将随粘土用量的增加而逐渐降低；当纳米级粘土的添加量从 0%增加到 6%时，弯曲强度从约 10 MPa 降低到约 6 MPa，但所有 UHTCC 的最大跨中挠度基本相同，约为 5 mm，说明适当掺量的纳米级粘土不会降低 UHTCC 的弯曲变形能力。2. 添加了 1%纳米级粘土的 UHTCC 的孔隙率最小（为 31.75%），阈值孔径为 183.13 nm，抗渗压力最大（为 1.8 MPa），且渗透时间最大（为 19 h）；其优异的抗渗性能可归因于纳米级粘土的填充和异质形核效应。3. 分散良好的纳米级粘土薄片使水分子渗透路径变得曲折，从而延长了渗水路程，但过量的纳米级粘土（>2%）会导致纳米团聚，并形成团簇缺陷，从而恶化抗渗性能。

关键词： 纳米粘土；渗透性；孔结构；水泥基复合材料；应变硬化